The complex, static displacement of a very long period seismic signal observed at Soufrière Hills volcano, Montserrat, WI

Dinko Šindija[a,*], Jürgen Neuberg[a], Patrick Smith[b,c]

[a]*School of Earth and Environment, University of Leeds, Leeds,* LS2 9JT, UK
[b]Montserrat Volcano Observatory, Flemmings, Montserrat, West Indies
[c]Now at: Dublin Institute for Advanced Studies, 5 Merrion Square, Dublin 2, Ireland

Abstract

In this study we demonstrate how very-long period (VLP) volcanic seismic signals can be processed in order to obtain essential and detailed information about the seismo-volcanic source process. As an example we use the VLP signal observed on 23 March 2012 during an outgassing event at Soufrière Hills volcano, Montserrat, acquired by instruments with different natural periods. The aim of this study is to highlight the importance of retrieving the correct source time function by a complete restitution process. When ground displacement cannot be retrieved through the restitution process due to very narrow band-pass limited instrument response, we compare synthetic and observed waveforms in the velocity domain and determine the best model by generating a synthetic velocity seismogram using the band-limited seismometer characteristics. Furthermore, we show how this approach of forward modelling can reveal much more detail of the source process, since small changes in displacement are enhanced in the velocity seismogram. Using these restituted and modelled displacements we perform a moment tensor inversion combined with a grid search locating the source at 600 m depth below sea level and estimating the source volume change to be in the range of

*Dinko Šindija

$0.6 - 1.1 \times 10^3$ m^3.

1. Introduction

Volcanogenic seismic signals cover a broad frequency range and fall into three main categories, and their interpretation and modelling are at the core of any attempt to forecast volcanic eruptions. Volcano-tectonic (VT) earthquakes, generated by the brittle failure of the rocks around the fault plane due to the stress changes of magmatic emplacement or due to pressure changes as a result of water-magma interaction in hydrothermal systems (Neuberg, 2020) have the same characteristics as tectonic earthquakes: clear P- and S-wave onsets and frequency content of 1-20 Hz. Low-frequency (LF) earthquakes have successfully been used in forecasting volcanic eruptions (e.g. Chouet, 1996). They have a spectral range between 0.2 and 10 Hz, with end members of the continuum being Long-Period (LP) events and hybrid events, which are similar to LP events but have additional high frequency onset (Neuberg, 2020). Their source processes differ significantly from the ones for generation of VTs. LF earthquakes originate at the boundary between magmatic fluid and solid surrounding rock (e.g. Chouet, 1988; Neuberg et al., 2000) or can be caused by slow, quasi-brittle low stress-drop failure driven by short-lived upper-edifice deformation (Bean et al., 2014). The deployment and widespread use of broadband seismic networks in the 1990s made studies of very-long period (VLP) signals possible (Kawakatsu et al., 1992; Neuberg et al., 1994) and we focus in our study on this category. VLP signals, whose periods range from several seconds to several minutes, have been observed on almost every type of volcano around the world (Chouet and Matoza, 2013). When the periods of these signals fall into the far end of the range they are often referred to as an ultra-long period (ULP) seismic signals. The event we are describing in this study falls into that range of ULPs, however we choose to call it a VLP as the source process between these two types of signals does not differ. Their source processes are usually attributed to fluid-rock interactions such as mass movement of volcanic fluids (e.g. Chouet and Dawson, 2011) generating abrupt pressure changes inside the volcanic edifice. As VLPs have been observed prior to caldera collapse (Kumagai et al., 2001; Michon et al., 2009) and prior to phreatic eruptions (Kawakatsu et al., 2000; Jolly et al., 2017) the need to study them is of great importance for understanding the underlying physical processes. Therefore, it is essential to retrieve the exact source time history in addition to amplitude and moment tensor components. The major advantage VLP signals offer is direct insight in the deformation of the source process. This fact was recognised and studied by Legrand et al. (2000, 2005). In this study we emphasise the importance of taking into account how different seismometers influence the observed signals and what the necessary processing steps are in order to retrieve the maximum amount of information from the observed waveforms. These processing steps go beyond the usual "instrument removal" applied as a routine by seismic processing packages, which considers the frequency range in the pass-band of the instrument only. In contrast, we try to retrieve information cut-out by the instrument and subsequently, use this information in our moment tensor inversion to estimate the location and mechanism of the source. As an example we use a VLP signal observed on 23 March 2012 during a outgassing event at Soufriére Hills volcano (SHV), Montserrat.

2. Data acquisition

At the time of the event the seismic network on the island of Montserrat consisted of nine stations equipped with three-component broadband seismometers. Due to recording problems, the number of stations available for this study was reduced to six: Waterworks (MBWW) station, deployed by the University of Leeds, equipped with a 120s Güralp-3T broadband instrument, Broderick's Yard (MBBY) and Windy Hill (MBWH) stations with 60s Güralp-3ESPC broadband instruments, and stations Fergus Ridge (MBFR), St. George's Hill (MBGH), and Roche's Yard (MBRY) equipped with 30s Güralp-40T broadband instruments (Figure 1). All data were recorded with a sampling rate of 100 Hz and were processed using the software package Obspy (Krischer et al., 2015).

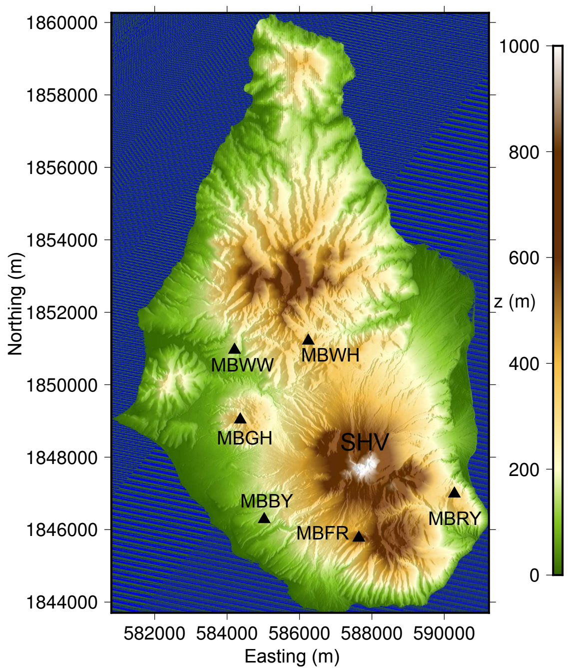

Figure 1: Topographic map of Montserrat with 6 operational stations on March 23, 2012

3. Seismicity on 23 March 2012

The eruption of SHV began in 1995 and has consisted of five phases of magma extrusion, the last of which ended on 11 February 2010. After more than two years of quiescence with no lava extrusion and low seismicity, two swarms of around 50 volcano-tectonic (VT) earthquakes occurred at SHV on 22 and 23 March 2012 (Smith, 2015). The most intense VT swarm lasted for around 15 minutes, starting at 07:10 UTC on 23 March 2012. During this swarm, a local magnitude (M_L) 3.9 VT earthquake was observed at 07:20 UTC making it the largest VT earthquake ever observed on Montserrat till that date (Cole et al., 2012). This was followed by three hybrid events that terminated the swarm at 07:22 UTC (Cole et al., 2012). A VLP signal was observed across the MVO (Montserrat Volcano Observatory) seismic network during this swarm coinciding with a large amplitude strain signal ($\sim$ 280 nano strain) recorded on borehole strainmeters on the island (Hautmann et al., 2014). Several hours after this swarm, a short episode of ash venting began and an elevated SO_2 flux was recorded between 23 and 27 March - peaking at 4600 t/day on 26 March 2012.

4. Data Processing

4.1. VLP signal identification

Although some VLP seismicity can be seen clearly on broadband velocity seismograms (e.g. Jolly et al., 2017), VLP signals often cannot easily be identified in the velocity domain. This is due to the instrument acting as a differentiator converting ground displacement to velocity, i.e. the instrument amplifies the high frequencies. Furthermore, a band-pass filter is applied defined by the instrument response. Often, the first step in searching for a VLP signal is analysing the amplitude spectrum of the velocity trace. In our example we see a broad peak relating to the VLP signal around 0.01 Hz (Figure 2a). However, this VLP signal has been distorted by the instrument response as the low frequencies in the original signal have been cut-off. Hence, when analysing VLP signals that have a frequency content outside the flat-band of the instrument response, one needs to keep in mind the original signal could contain seismic energy at much longer periods than displayed in the amplitude spectrum of the recorded signal. Figure 2b shows such an example where a signal with dominant period of 500s is observed at the station with the 120 second instrument.

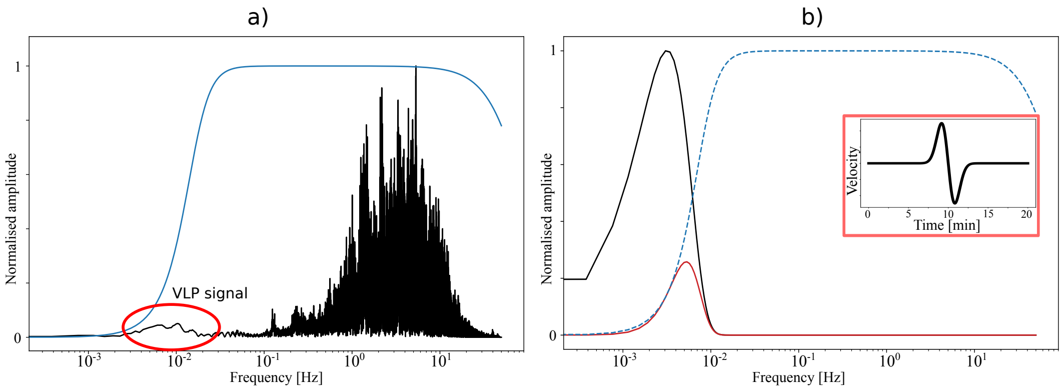

Figure 2: a) Amplitude spectrum of the vertical component velocity seismogram recorded at MBWW station on March 23, 2012 showing a broad VLP signal with dominant frequency of 0.01 Hz with superimposed transfer function of 120s-instrument at that station. b) Example of how the instrument response impacts the observed amplitude spectrum. We produced a synthetic velocity seismogram with period of 500 seconds (red box), calculated the amplitude spectrum (black) and then simulated the effect of the 120s-instrument response on the input signal (red).

Another simple way to identify a VLP signal when it is not directly observable on the velocity seismogram is to integrate the velocity seismogram or apply a low-pass filter. Figure 3a shows a 16 minute long record of the VT swarm observed on 23 March 2012. The velocity seismogram is dominated by the high frequency VT earthquakes. However, if we integrate the seismogram (Figure 3b) the VLP signal becomes obvious. In this case we see two clear VLP signals, one starting at 07:16 UTC and the other one, with much larger amplitude, at 07:19 UTC. In this study we focus on the second, larger amplitude signal.

4.2. Restitution of the ground displacement

To account for the shape of the instrument response and to make sure that the restitution of ground displacement considers the whole energy content of the ground motion we have to carry out certain processing steps. The process of restitution of the ground displacement is depicted in Figure 3. We apply different high-pass filters with cut-off frequencies of 0.004 Hz, 0.002 Hz, and 0.001 Hz to the velocity trace after which we remove the instrument response (including the digitiser gain) and integrate the trace to obtain the displacement seismogram (Figure 3 c-e). The application of a high-pass filter with a cut-off frequency lower than the flat-band of the instrument response (Neuberg and Luckett, 1996; Caudron et al., 2018) helps us recover the low frequency information while suppressing the amplification of the long period, environmental and electronic noise during the integration. Choosing the appropriate high pass filter is crucial, as the interpretation of the obtained displacement seismograms changes. Trace (c) shows with an apparent inflation (motion up) followed by a deflation (motion down) below the original level. This interpretation dramatically changes by including longer periods in traces (d) and (e). The ground displacement shown now in trace (e) could be described as a step-like inflation. The fact that a further extension to a lower frequency range does not change the waveform indicates that the trace now represents the “true” ground displacement of the process. In this case it gives us the “true” amplitude of the displacement as well, which can be directly read from the displacement seismogram (Figure 3f). Unfortunately there is no general recipe or criteria how to define the lowest cut-off frequency as this process highly depends on the data quality. In general, the vertical components are less affected by low frequency noise than the horizontal components. We also have to assume that there is no seismic energy or a static offset at even lower frequencies.

The restitution process comprises the application of the inverse instrument transfer function using complex Poles and Zeros (PAZ) response files provided by the manufacturer. The integration from velocity to displacement can be carried separately or by including an extra term $(s-0)$ in the inverse instrument transfer function (Scherbaum, 2001)

$$\mathcal{U}_{\mathrm{g}} = c' \frac{(s-p_1)(s-p_2)(s-p_3)\cdots(s-p_{\mathrm{np}})}{(s-z_1)(s-z_2)(s-z_3)\cdots(s-z_{\mathrm{nz}})(s-0)} \mathcal{X}_{\mathrm{vel}}, \tag{1}$$

where $\mathcal{U}_{\mathrm{g}}$ is the displacement seismogram, $\mathcal{X}_{\mathrm{vel}}$ the recorded velocity seismogram, nz is number of zeros z and np is number of poles p, while c' is the overall normalisation constant containing also the digitiser gain.

4.3. Forward modelling of ground displacement

Due to the very low frequency content in our example, this restitution method was not applicable for the stations equipped with instruments with natural periods shorter than 120 s. These instruments have a much lower signal to noise ratio at long periods. A way around this problem is using the following forward modelling technique: we assume a ground displacement model, or adopt the one determined by the 120s instrument as a starting model. Next we apply the instrument response of 60s or 30s seismometers to this trace and compare the resulting synthetic velocity seismogram with the velocity data. This is done similarly to the restitution process, however when we apply the instrument response (i.e. multiplying the displacement model with the transfer function, hence simulating the recording

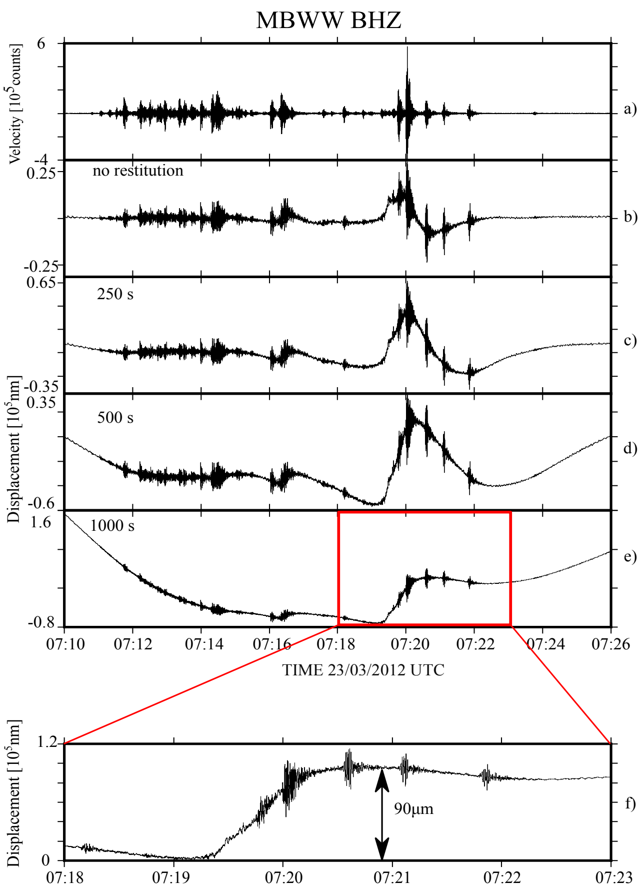

Figure 3: Restitution of the vertical component ground displacement at MBWW station. (a) Uncorrected velocity seismogram. (b) Integrated (without restitution) velocity seismogram which identifies the VLP signal (c) to (e) Displacement seismograms after correcting for the instrument response and considering spectral components to a period of 250, 500 and 1000 s respectively. (f) Five minute long time window showing true ground displacement.

process), an extra Zero in our PAZ response files equals differentiation when we move from the displacement to the velocity domain. As a starting model for ground displacement we use an approximation of the waveform that we obtained from the vertical component of the 120 s instrument at the MBWW station. Vertical components are generally less affected by the noise than the horizontal components. One has to be aware that such an approach makes all following results highly dependent on the single station MBWW. If the instrument response is even slightly incorrect the effect will be carried across the network into all synthetic displacement seismograms and, therefore, into the model. Similarly, any other noise at MBWW would be carried through to the rest of the stations.

In the limited 5 min time window shown in Figure 3f, the restituted signal appears to be a step function, however, outside this time window the long term behaviour cannot be uniquely determined. As the signal was recorded with a velocity sensor (seismometer) a static offset represented by the step function will always decay to zero. Nevertheless, focusing on the source process in our volcanological study, we are interested in the initial slope of the signal. Therefore, in contrast to VLP signals on other volcanoes that are observed and interpreted as oscillatory behaviour (e.g. Dawson and Chouet, 2014; Caudron et al., 2018), we assume the model of a step-like displacement. We model it by using the Richards Growth Equation (RGE), a generalised logistic function defined by upper (K) and lower (A) asymptotes, the curve growth rate (B), the time of the maximum growth (M), and the asymmetry parameter (ν) (Richards, 1959; Green and Neuberg, 2005):

$$Y(t) = A + \frac{K - A}{[1 + e^{B(t-M)}]^{1/\nu}}. \tag{2}$$

We adjust the parameters of the step function to match the restituted ground displacement of the vertical component of the 120s instrument (Figure 4). This trace is now used as input to create the synthetic velocity seismograms for the 120s, 60s, and 30s instruments, respectively. First we apply the 120s instrument response (including differentiation), apply a low-pass filter and compare it with the low-passed data of MBWW (Figure 4). The comparison shows that even though the amplitude of the step function is well constrained by the restituted data from the MBWW station, the modelled step function does not match the detailed time history in the velocity domain. The same discrepancy is also seen when comparing the resulting velocity seismograms of the band-limited stations with the original data on other components and stations. Upon more detailed analysis of the restituted ground displacement at MBWW we noticed a change of slope in the step function approximately 1.5 minutes (t_0) into the trace. To model this discontinuity, we designed a two-phase step function using the RGE as a basis to see if a change in the slope can explain the discrepancy in the velocity domain. The modified step function is therefore divided into two phases, Y_{phase1} and Y_{phase2} (Figure 4) described respectively as:

$$Y_{\text{phase1}}(t) = A_1 + \frac{K_1 - A_1}{[1 + e^{B_1(t-M_1)}]^{1/\nu_1}},\ t \leq t_0 \tag{3}$$

$$Y_{\text{phase2}}(t) = A_2 + \frac{K_2 - A_2}{[1 + e^{B_2(t-M_2)}]^{\nu_2}},\ t > t_0. \tag{4}$$

A crucial assumption we make is that the change in the slope happens at the same time for all components at all stations. Due to the wavelength of the signal, the arrival time difference at different station is negligible, therefore we can take this assumption into an account. The function is made continuous by selecting A_2 which minimises $|\max(Y_{\text{phase1}}) - \min(Y_{\text{phase2}})|$. Applying the instrument response to this model for ground displacement produces a synthetic velocity seismogram which better matches the data in the velocity domain. Now that we have shown this model works for a station equipped with 120s instrument, we examine how well our ground displacement model fits at stations equipped with 60 s and 30 s instruments. While for station MBWW the displacement model is fitted to the restituted ground displacement, for other stations we use the simulated annealing

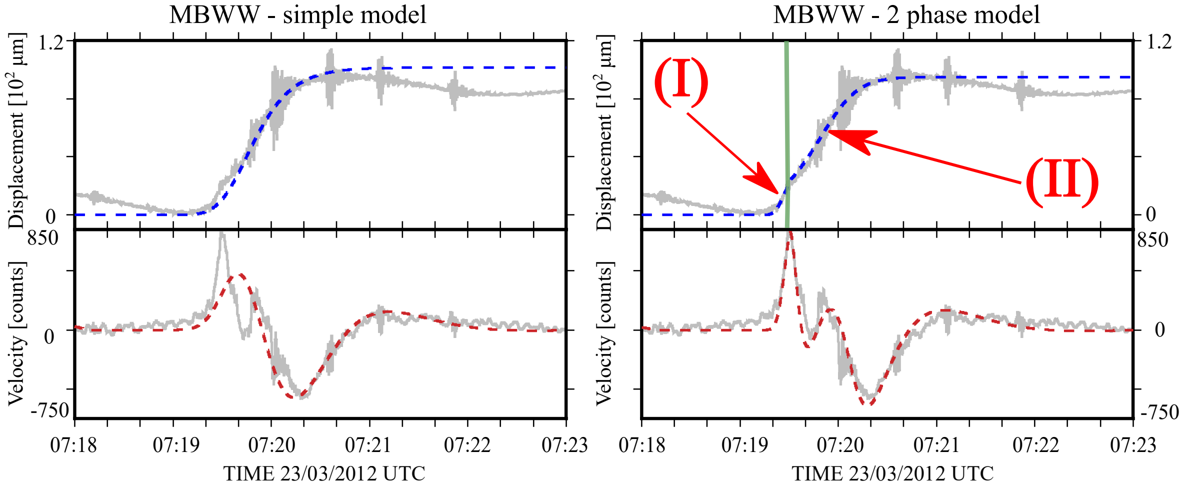

Figure 4: Ground displacement models (blue dashed lines) based on the restituted ground displacement (grey) at MBWW on March 23, 2012; using a simple step function (left) and using a 2 phase step function (right). We apply the band-pass limited instrument response and differentiate both ground displacement models and then compare the resulting synthetic velocity data (red dashed line) with the low passed filtered (below 20s) observed data (grey). The green vertical line represents the onset time of the change of slope and the roman numerals represent the two phases of our modeled step function.

(SA) method (Du and Swamy, 2016) to determine the best fit. We vary the ground displacement model parameters and the goodness of a fit is measured in the velocity domain. A 95 % confidence interval has been included in the overall step amplitude estimate. Therefore, a 10% uncertainty in the estimate of the step amplitude linearly translates into 10 % uncertainty in the volume change estimate in Section 5.2. Using the method of Wielandt and Forbriger (1999) we also removed the effect of the tilt from the horizontal components. Our results show that the two-step model can explain the observed velocity waveforms on all available stations in the network for both the vertical and horizontal components (Figure 5, Appendix A). Furthermore, the results from 60 and 30 s stations reinforce our selection of the 1000 s high-pass filter as an appropriate one for the restitution process because if our ground displacement were not a step-like function it would not provide the very good match in the velocity domain. While the combined fit in velocity and displacement domain was necessary to circumvent the band-width limitations of 30 and 60s instruments, this approach also revealed the advantages capturing details in the time history of the signal in the velocity domain.

5. Source mechanism and location

5.1. Method

Only after we perform the appropriate restitution process, obtaining the amplitude and time history of the observed displacements, can we evaluate the volume change at the source by performing a moment tensor inversion (MTI) using the software package VOLPIS (Cesca and Dahm, 2008). By using this method we can resolve both the moment tensor (MT) and single force (SF) components as well as the source time history. As we are mostly interested in the combined amplitude of the two-phase source displacement, we model the static displacement again as a simple step function (Equation 2). These are modelled individually for each component at each station based on the two-phase step function so the start, end, and the maximum amplitude of the static displacement is equal. Additionally, as VOLPIS is a frequency domain inversion code, the large static step at the end of our displacement models makes the inversion unstable. Therefore we differentiate

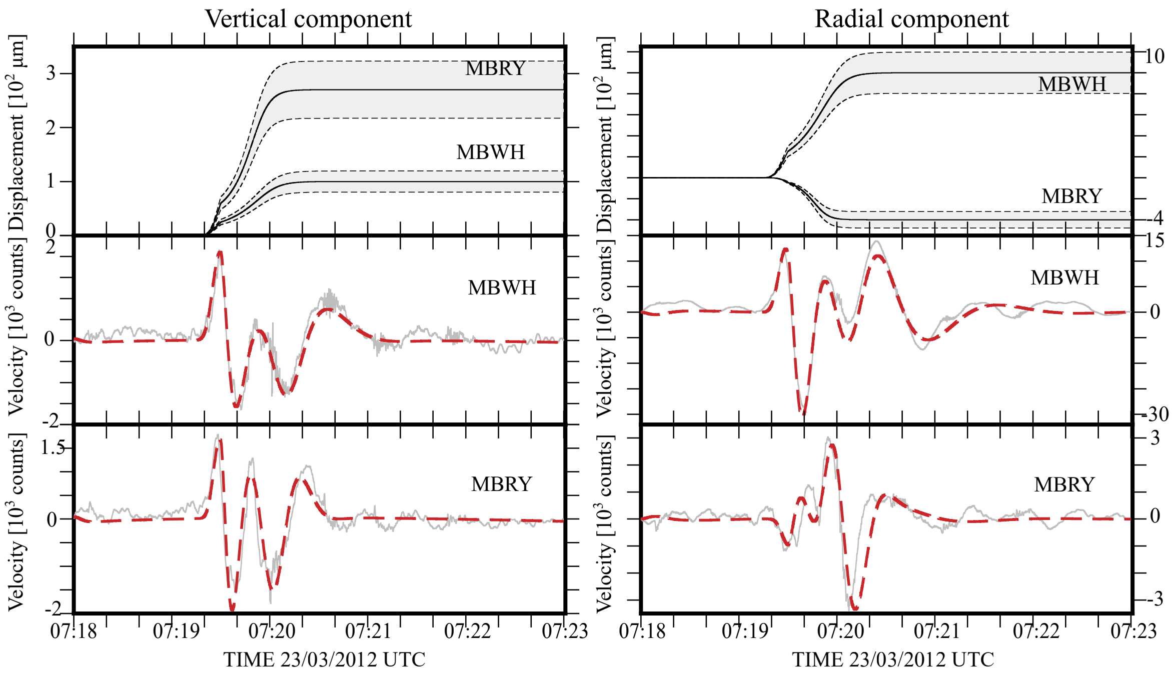

Figure 5: Vertical (left) and radial (right) component of the modelled ground displacements for stations MBWH and MBRY using the 2 phase step functions. The 95 % confidence intervals are shown as grey shaded areas. After simulating the instrument response we compare the synthetic velocity data (red dashed line) with the observed data (grey). Low-pass filter with cut-off frequency of 20s is applied to both synthetic and observed data.

the resulting displacement step models:

$$v(t) = \frac{d}{dt}Y(t) = \mathcal{F}^{-1}\left[j\omega\mathcal{Y}(\omega)\right], \; \mathcal{Y}(\omega) = \mathcal{F}\left[Y(t)\right] \tag{5}$$

where $v(t)$ represents the velocity trace, $Y(t)$ is a simple step function, and the $\mathcal{F}$ indicates the Fourier transform. The MTI is therefore performed in the velocity domain resulting in the moment rate components. The resolved moment rate components are then integrated and can be directly compared with the source time history used for modelled displacements. The Green's functions are computed using a spectral element method SPECFEM3D (Komatitsch et al., 2012), for a volumetric grid (2.0km × 1.2km × 0.8km) (Figure 6) of possible source locations with grid spacing of 200 m centred below the summit of SHV. The topography is included in the calculation of the Green's functions assuming a homogeneous halfspace with $v_{\mathrm{p}} = 3500$ m/s, $v_{\mathrm{s}} = 2000$ m/s, and $\rho = 2600$ kg/m^3. As the VLP signals have wavelengths much larger than the source-receiver distances, we do not expect any influence from subsurface heterogeneities, and the assumption of a homogeneous halfspace is justified. We perform the MTI for each point in the grid and estimate the location of the source by finding the minimum misfit between observed displacement seismograms and obtained synthetic displacement seismograms through our inversion using:

$$\mathrm{misfit} = \left[\frac{\sum_{\mathrm{i=1}}^{\mathrm{N_t}} \sum_{\mathrm{j=1}}^{\mathrm{M_i}} (\mathrm{d_i(t_j)} - \mathrm{s_i(t_j)})^2}{\sum_{\mathrm{i=1}}^{\mathrm{N_t}} \sum_{\mathrm{j=1}}^{\mathrm{M_i}} (\mathrm{d_i(t_j)})^2} \right], \tag{6}$$

where N_t is the number of time traces, M_i is the number of time samples for j-th trace, and $d_i(t_j)$ and $s_i(t_j)$ are the j-th samples of i-th time trace for input data and synthetic time trace respectively (Cesca and Dahm, 2008). The misfit results are dimensionless and normalised. The data were downsampled to 3 Hz and bandpassed between 0.001 and 1 Hz. The inversions are done whilst keeping the constraint for the source parameters to have same time histories for the MT and SF components.

5.2. Results

The best-fitting model was located to be at depth of 600 m, 1000 m east and 400 m south of the volcano summit (Figure 6). The resulting waveform fit (Figure

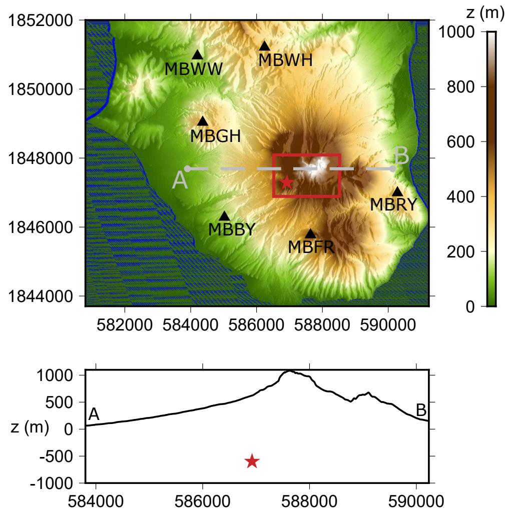

Figure 6: (top) Zoomed in map of Montserrat showing the horizontal boundaries of the volumetric grid of possible source locations (red triangle). Location of the best-fitting model is shown with the red star. (bottom) Cross section profile (extracted from point A to point B) showing the depth of the source and its relative location from the summit of the SHV.

7) shows a fairly good fit for all three components at all stations. The resulting moment and single force rate time histories are shown in Figures 8. By normalising the resolved moment tensor (Figure 8):

$$\boldsymbol{M} = M_0 \begin{bmatrix} M_{\mathrm{nn}} & M_{\mathrm{ne}} & M_{\mathrm{nz}} \\ M_{\mathrm{en}} & M_{\mathrm{ee}} & M_{\mathrm{ez}} \\ M_{\mathrm{zn}} & M_{\mathrm{ze}} & M_{\mathrm{zz}} \end{bmatrix} = 3.8 \times 10^{13} \begin{bmatrix} 0.53 & -0.29 & -0.55 \\ -0.29 & 0.13 & -0.44 \\ -0.55 & -0.44 & 0.73 \end{bmatrix} \mathrm{Nm} \qquad (7)$$

we estimate the scalar seismic moment to be 3.8×10^{13} Nm. The resolved vector of single forces is:

$$\boldsymbol{F} = F_0 \begin{bmatrix} F_{\mathrm{n}} \\ F_{\mathrm{e}} \\ F_{\mathrm{z}} \end{bmatrix} = 3.3 \times 10^{10} \begin{bmatrix} 0.17 \\ -0.75 \\ -0.64 \end{bmatrix} \mathrm{N} \qquad (8)$$

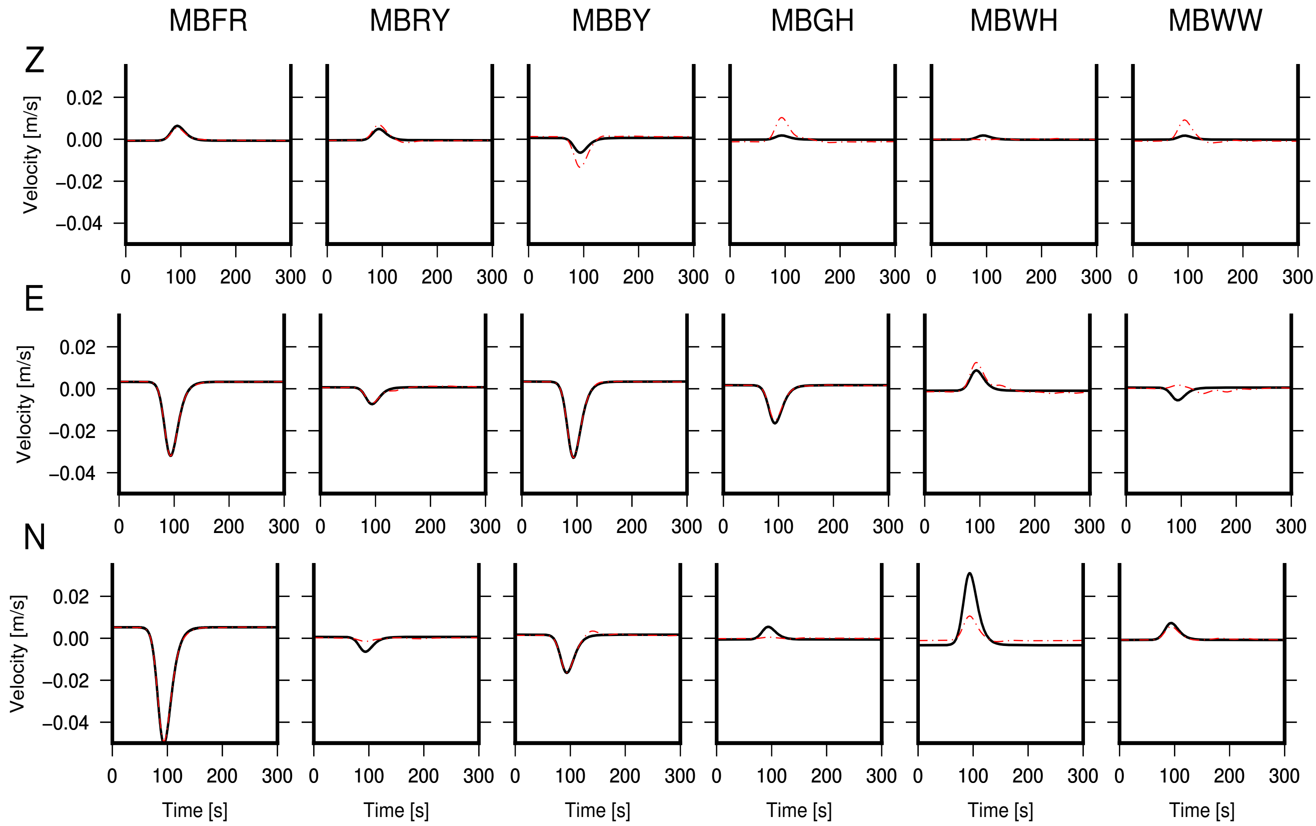

Figure 7: The seismogram fit in the velocity for three components at the available stations for the March 2012 event. Black solid line represents our input data for the inversion, while the dashed red line represents the best-fit solution synthetic data.

Comparing the maximum amplitudes of single force components (8) and their moment counterparts we see that $|\frac{SF_{\mathrm{north}}}{M_{\mathrm{xx}}}| = 0.0003\ \mathrm{m}^{-1}$, $|\frac{SF_{\mathrm{east}}}{M_{\mathrm{yy}}}| = 0.005\ \mathrm{m}^{-1}$, and $|\frac{SF_{\mathrm{vert}}}{M_{\mathrm{zz}}}| = 0.0007\ \mathrm{m}^{-1}$ demonstrating that the single force components are negligible. We follow the decomposition of the resolved moment tensor by Vavryčuk (2001) and calculate the percentage of isotropic component to be 64%, CLVD component 12%, and double couple component to be 24%. The shear component has a strike of 187°, dip 21°, and rake 146°. The volume change (ΔV) at the source is then estimated using $\Delta V = \frac{M_{\mathrm{iso}}}{(\lambda + \frac{2}{3}\mu)}$, where M_{iso} represent isotropic moment and λ and μ are Lamé parameters. Assuming a Poisson's ratio $\nu = \frac{1}{4}$ ($\lambda = \mu$) and our model space velocities, we estimate the source volume change to be $\Delta V = (1015 \pm 100)$ m^3. However, for volcanic rocks at or near liquidus temperature it may be more appropriate to use a Poisson's ratio $\nu = \frac{1}{3}$ ($\lambda = 2\mu$) (Murase and McBirney, 1973) which results in a source volume change $\Delta V = (635 \pm 60)$ m^3.

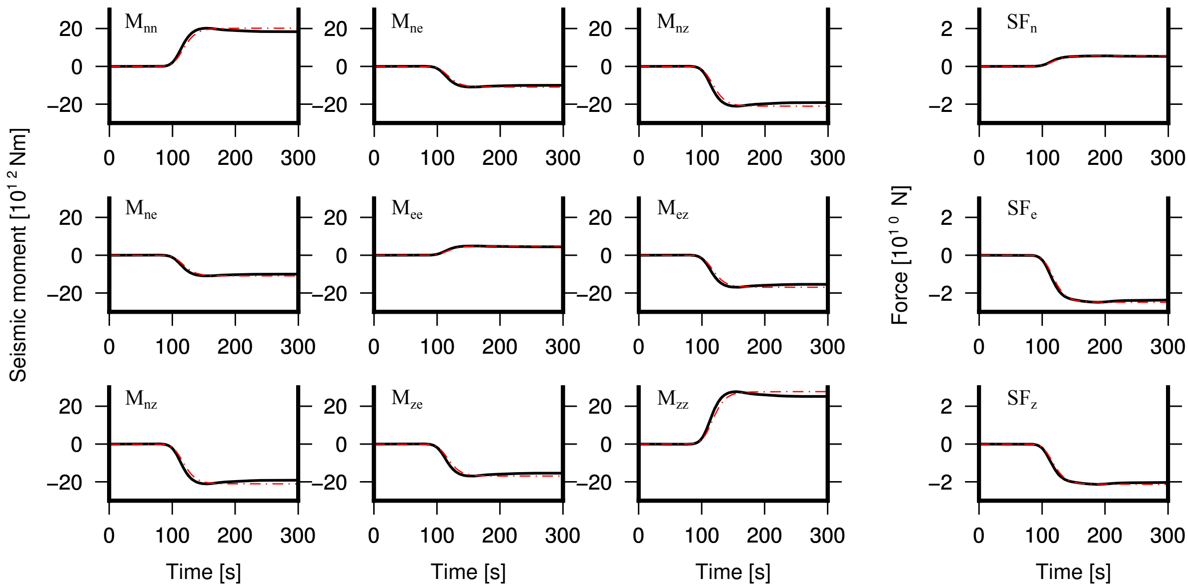

Figure 8: The resolved source time histories for the moment tensor and single force components (black). We multiply the average source time function used for the modelled displacements with the moment tensor/ single force component (dashed red line) so we can compare how well the shape of the displacement step function is resolved.

6. Discussion

This event demonstrates the need to include in the restitution of ground displacement the spectral components of the VLP signal that go beyond the natural period of the seismometer. When ground displacements cannot be retrieved through a restitution process, we show how by modelling ground displacements and accounting for the seismometer response, we can compare synthetic and observed waveforms in the velocity domain and determine the best model. Additionally, we show in our example how forward modelling can reveal more details of the source process, since small changes in displacement are enhanced in the velocity domain. As VLP signals have wavelengths of 10s to 100s of km, it places all of our seismic stations in the so-called near-field, i.e. within one wavelength from the source. In the near-field, the seismic displacement at the surface is directly proportional to the deformation at the source. In our example, where we observe a signal with a dominant period of approximately 100 s, equivalent to a wavelength of 350 km, all stations are in the near field and we can relate our restituted displacement and models to a source volume change. The two-phase step function describing the displacement at the source, has not been seen in such detail before. The result implies that the source volume change happened in two-phases, a rapid onset and then a slower continuation of the motion. We cannot say whether this type of motion is due to the source itself acting in two phases or whether the slower continuation of the motion is due to a rebound effect of the surrounding medium, however this question lies outside the scope of this study. This process differs from a previous VLP observed on SHV Green and Neuberg (2005) which had larger observed displacements but a simpler source time history. Unlike the signal analysed by Green and Neuberg (2005) where only vertical component seismograms at two stations were used, this event was observed on all three components at six stations in the seismic network. Although the azimuthal coverage of the network was not perfect, the observations still show that the same source time history can be seen on all components. It also allows us to perform moment tensor inversion to improve our interpretation of the source mechanics, although it is necessary to consider the effect of the network coverage in the estimation of the source mechanism and source volume change. If the inversions do not converge to a unique solution, we still could have a good fit in the displacement/velocity domain, however the resolved MT/SF components could not be resolved. We can directly relate the observations at the surface to the source mechanism, by comparing the inverted time histories of moment tensor and single force components with the modelled source time function and, hence, obtain another verification of our moment tensor inversion result. Those show the source mechanism of the best-fitting model is an explosion with a strong shear component (Figures 8). The source volume change for the best fitting model is estimated to be in the range of $0.6 - 1.1 \times 10^3$ m^3. Using strain data from 3 borehole dilatometers, Hautmann et al. (2014) described this ash venting event as being initiated by the ascent of magmatic fluid from deeper magmatic system into shallow dyke. However, based on our estimate of volume change and depth we can speculate that it is not the sudden movement of magma that initiated this event, but rather it was due to CO_2 flushing. If an amount of free gas phase of CO_2, degassing at larger depths, hits a supersaturated magma batch it can get the water out of the solution and cause a sudden volume change (Caricchi et al., 2018). Looking at a broader aspect of the previous eruptive behaviour of SHV, such modulations could have been a trigger for the onset of a new eruptive phase which would explain why it is not the overpressure or a certain volume recharge that needs to be reached to start an eruptive phase (Figure 9).

7. Conclusions

The analysis of the VLP signal observed on 23 March 2012 during an outgassing and ash-venting event on Soufriére Hills Volcano, Montserrat provides a great ex-

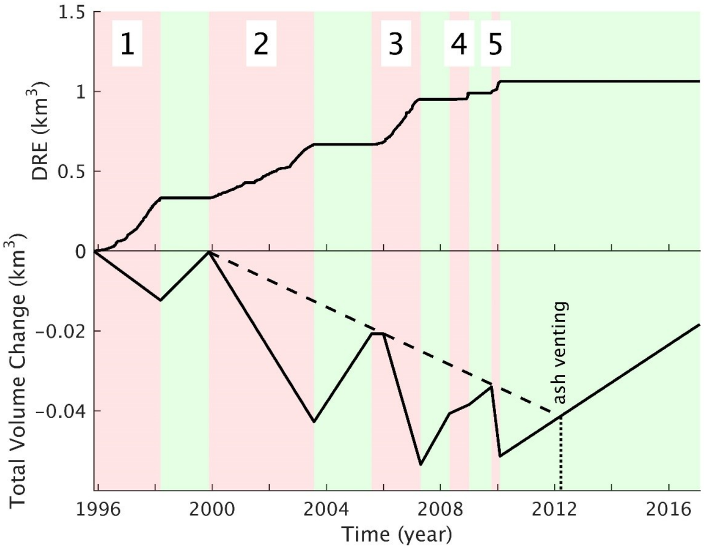

Figure 9: *Approximation of the cumulative source volume change since the start of the eruption in 1995. The volume extruded during eruptive phase always exceeds the volume replenished during quiet periods. The dashed line marks the onset of renewed extrusions and links it to the timing of the ash-venting episode studied here. Adapted from Neuberg et al. (2018)*

ample how the VLP signals can and should be processed. It is of great importance to carry out the proper processing steps in order to retrieve the maximum amount of information from the observed seismograms if we want to interpret source mechanism of VLP signals correctly. We show how forward modelling of the ground displacement can reveal much more details of the source process, since the small changers in displacement are enhanced in the velocity seismogram. Additionally we perform moment tensor inversions and estimate the source mechanism to be an isotropic mechanism with a strong shear component. The resulting volume change, potentially caused by CO_2 flushing is estimated to be in the range of $0.6 - 1.1 \times 10^3$ m^3. By combining the results from our restitution process, forward modelling, and the moment tensor inversion we interpret the source mechanism of the event to be an volume opening with a complex, static source displacement with a strong shear component acting in a two-phase motion with a rapid onset and a slower continuation of the motion.

Acknowledgments

D. Šindija is funded by the University of Leeds Research Scholarship. J. Neuberg is partly funded by the Centre for the Observation and Modelling of Earthquakes, Volcanoes and Tectonics (COMET NE/J01978X/1). The seismic data is curated by Montserrat Volcano Observatory and can be made available upon request to mvo@mvo.ms. This work was undertaken on ARC3, part of the High Performance Computing facilities at the University of Leeds, UK. We thank the two anonymous reviewers for their insightful comments that improved the original manuscript.

References

Bean, C.J., De Barros, L., Lokmer, I., Métaxian, J.P., O'Brien, G., Murphy, S., 2014. Long-period seismicity in the shallow volcanic edifice formed from slow-rupture earthquakes. Nature Geoscience 7, 71–75.

Caricchi, L., Sheldrake, T.E., Blundy, J., 2018. Modulation of magmatic processes by CO_2 flushing. Earth and Planetary Science Letters 491, 160–171.

Caudron, C., Taisne, B., Neuberg, J., Jolly, A.D., Christenson, B., Lecocq, T., Suparjan, Syahbana, D., Suantika, G., 2018. Anatomy of phreatic eruptions. Earth, Planets and Space 70, 168.

Cesca, S., Dahm, T., 2008. A frequency domain inversion code to retrieve time-dependent parameters of very long period volcanic sources. Computers & Geosciences 34, 235–246.

Chouet, B., 1988. Resonance of a fluid-driven crack: Radiation properties and implications for the source of long-period events and harmonic tremor. Journal of Geophysical Research: Solid Earth 93, 4375–4400.

Chouet, B., Dawson, P., 2011. Shallow conduit system at Kilauea Volcano, Hawaii, revealed by seismic signals associated with degassing bursts. Journal of Geophysical Research: Solid Earth 116.

Chouet, B., Matoza, R., 2013. A multi-decadal view of seismic methods for detecting precursors of magma movement and eruption. Journal of Volcanology and Geothermal Research 252, 108 – 175.

Chouet, B.A., 1996. Long-period volcano seismicity: its source and use in eruption forecasting. Nature 380, 309–316.

Cole, P., Bass, V., Christopher, T., Odbert, H., Smith, P., R., S., Stinton, A., Syers, R., Williams, P., 2012. MVO scientific report for volcanic activity between 1 November 2011 and 30 April 2012.

Dawson, P., Chouet, B., 2014. Characterization of very-long-period seismicity accompanying summit activity at Ka'lauea Volcano, Hawai'i: 2007-2013. Journal of Volcanology and Geothermal Research 278-279, 59.

Du, K.L., Swamy, M.N.S., 2016. Simulated Annealing. Springer International Publishing, Cham. pp. 29–36.

Green, D.N., Neuberg, J., 2005. Seismic and infrasonic signals associated with an unusual collapse event at the Soufrière Hills volcano, Montserrat. Geophysical Research Letters 32, L07308.

Hautmann, S., Witham, F., Christopher, T., Cole, P., Linde, A.T., Sacks, I.S., Sparks, R.S.J., 2014. Strain field analysis on Montserrat (W.I.) as tool for assessing permeable flow paths in the magmatic system of Soufrière Hills volcano. Geochemistry, Geophysics, Geosystems 15, 676–690.

Jolly, A., Lokmer, I., Thun, J., Salichon, J., Fry, B., Chardot, L., 2017. Insights into fluid transport mechanisms at White Island from analysis of coupled very long-period (VLP), long-period (LP) and high-frequency (HF) earthquakes. Journal of Volcanology and Geothermal Research .

Kawakatsu, H., Kaneshima, S., Matsubayashi, H., Ohminato, T., Sudo, Y., Tsutsui, T., Uhira, K., Yamasato, H., Ito, H., Legrand, D., 2000. Aso94: Aso seismic observation with broadband instruments. Journal of Volcanology and Geothermal Research 101, 129–154.

Kawakatsu, H., Ohminato, T., Ito, H., Kuwahara, Y., Kato, T., Tsuruga, K., Honda, S., Yomogida, K., 1992. Broadband seismic observation at the Sakurajima volcano, Japan. Geophysical Research Letters 19, 1959–1962.

Komatitsch, D., Vilotte, J.P., Tromp, J., Ampuero, J.P., Bai, K., Basini, P., Blitz, C., Bozdag, E., Casarotti, E., Charles, J., Chen, M., Galvez, P., Goddeke, D., Hjorleifsdottir, V., Labarta, J., Le Goff, N., Le Loher, P., Lefebvre, M., Liu, Q., Luo, Y., Maggi, A., Magnoni, F., Martin, R., Matzen, R., McRitchie, D., Meschede, M., Messmer, P., Michea, D., Nadh Somala, S., Nissen-Meyer, T., Peter, D., Rietmann, M., de Andrade, E., Savage, B., Schuberth, B., Sieminski, A., Strand, L., Tape, C., Xie, Z., Zhu, H., 2012. Specfem3d cartesian v2.0.2 [software]. doi:http://doi.org/NoDOI.

Krischer, L., Megies, T., Barsch, R., Beyreuther, M., Lecocq, T., Caudron, C., Wassermann, J., 2015. Obspy: a bridge for seismology into the scientific Python ecosystem. Computational Science and Discovery 8, 014003.

Kumagai, H., Ohminato, T., Nakano, M., Ooi, M., Kubo, A., Inoue, H., Oikawa, J., 2001. Very-long-period seismic signals and caldera formation at Miyake Island, Japan. Science 293, 687–690.

Legrand, D., Kaneshima, S., Kawakatsu, H., 2000. Moment tensor analysis of near-field broadband waveforms observed at Aso Volcano, Japan. Journal of volcanology and geothermal research 101, 155–169.

Legrand, D., Rouland, D., Frogneux, M., Carniel, R., Charley, D., Roult, G., Robin, C., 2005. Interpretation of very long period tremors at Ambrym volcano, Vanuatu, as quasi-static displacement field related to two distinct magmatic sources. Geophysical research letters 32.

Michon, L., Villeneuve, N., Catry, T., Merle, O., 2009. How summit calderas collapse on basaltic volcanoes: New insights from the april 2007 caldera collapse of Piton de la Fournaise volcano. Journal of Volcanology and Geothermal Research 184, 138–151.

Murase, T., McBirney, A.R., 1973. Properties of some common igneous rocks and their melts at high temperatures. Geological Society of America Bulletin 84, 3563–3592.

Neuberg, J., Barclay, J., Burton, M., Calder, E., Fournier, N., Rivalta, E., 2018. Assessment of the hazards and risks associated with the Soufrière Hills Volcano, Montserrat. 22nd Report of the Scientific Advisory Committee on Montserrat Volcanic Activity (Full Report) .

Neuberg, J., Luckett, R., 1996. Seismo-volcanic sources on Stromboli volcano .

Neuberg, J., Luckett, R., Baptie, B., Olsen, K., 2000. Models of tremor and low-frequency earthquake swarms on Montserrat. Journal of Volcanology and Geothermal Research 101, 83 – 104.

Neuberg, J., Luckett, R., Ripepe, M., Braun, T., 1994. Highlights from a seismic broadband array on Stromboli volcano. Geophysical Research Letters 21, 749–752.

Neuberg, J.W., 2020. Earthquakes, Volcanogenic. Springer International Publishing, Cham. pp. 1–10.

Richards, F.J., 1959. A flexible growth function for empirical use. Journal of Experimental Botany 10, 290–300.

Scherbaum, F., 2001. Of poles and zeros: fundamentals of digital seismology. volume 15. 2nd ed., Kluwer Academic, Dordrecht;London;.

Smith, P., 2015. Volcano-tectonic seismicity of Soufriere Hills volcano, Montserrat. Encyclopedia of Earthquake Engineering , 3907–3919.

Vavryčuk, V., 2001. Inversion for parameters of tensile earthquakes. Journal of Geophysical Research: Solid Earth 106, 16339–16355. URL: http://dx.doi.org/10.1029/2001JB000372, doi:10.1029/2001JB000372.

Wielandt, E., Forbriger, T., 1999. Near-field seismic displacement and tilt associated with the explosive activity of Stromboli. Annals of Geophysics 42.

Appendices

Appendix A

Here we show the residual seismogram from the Wielandt and Forbriger (1999) method for tilt removal. Figure 10 shows the removal of the tilt component at station MBWW. After the tilt is removed from the horizontal components we rotate the seismograms back to north and east seismograms. The effect of the tilt signal is shown in Figure 11 for the north component at MBWW.

Appendix B

Figures 12 and 13 show the displacement models for all three components and at all stations. We apply the seismometer response to these models and then compare it with the band-passed velocity seismograms. Both the synthetic and original velocity seismograms are filtered between 20 and 1000 seconds. The horizontal components are rotated into radial and transverse components, then we remove the influence of tilt signals, after which the resulting traces are rotated back into east and north components. The backazimuth is derived from the particle motion using the horizontal components.

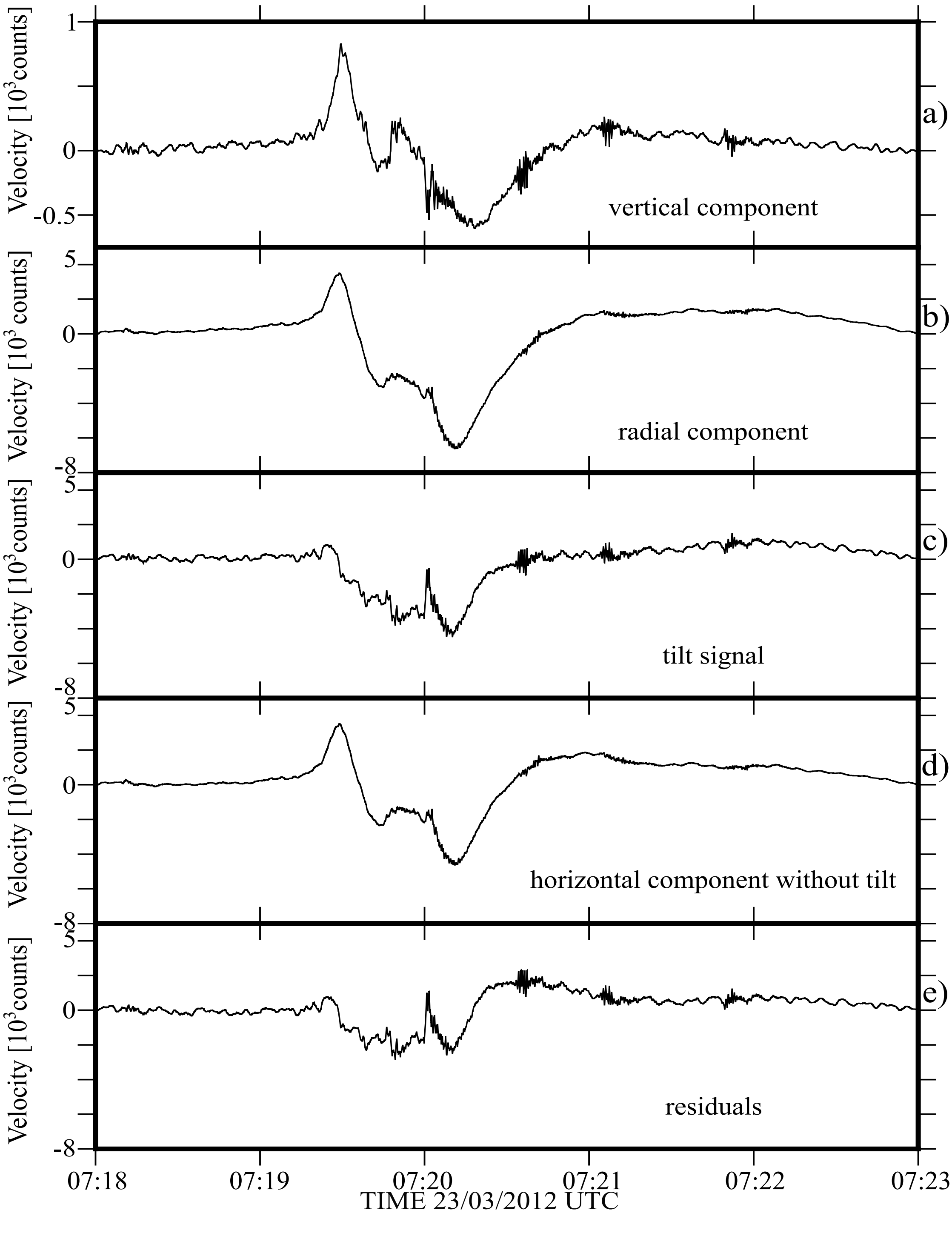

Figure 10: Trace a) is the vertical component velocity trace band-passed between 1000 and 20s. Traces c) and d) show the radial component after removal of the displacement and tilt component respectively, and e) shows the residual after removing both components from the horizontal trace.

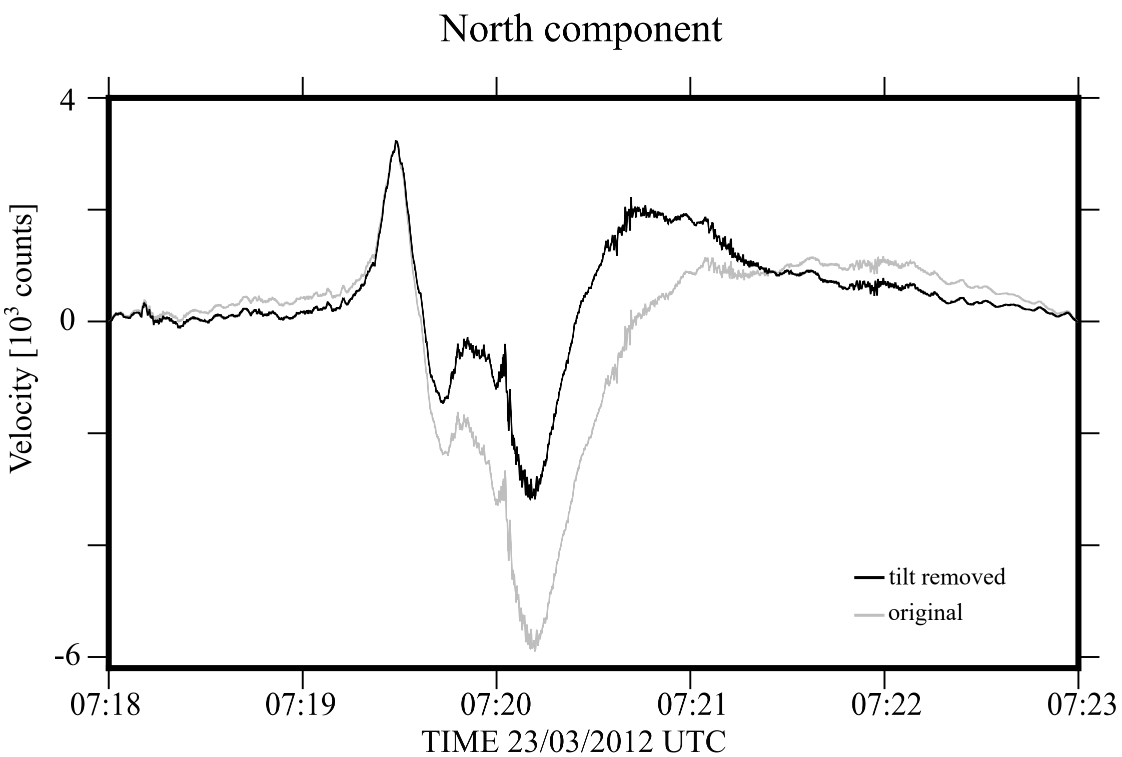

Figure 11: North component velocity seismogram at MBWW station before (grey) and after (black) removal of the tilt.

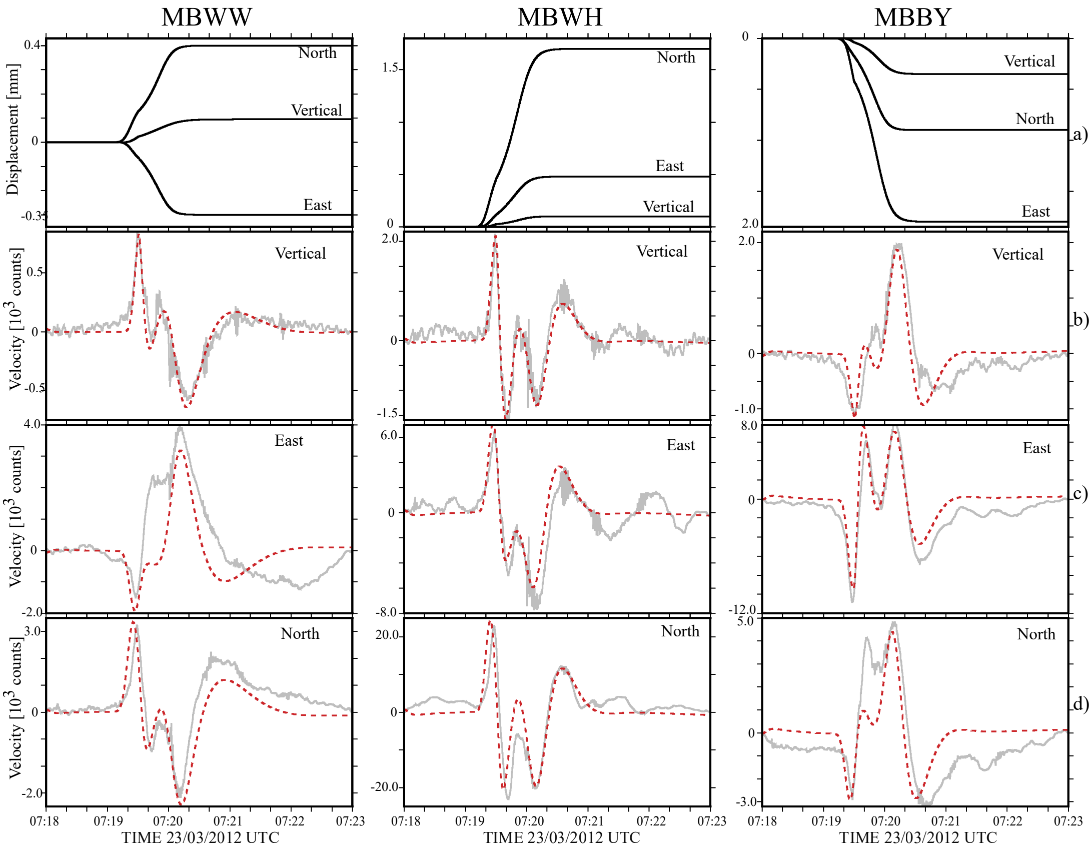

Figure 12: (a) Displacement models for all three components at stations MBWW, MBWH, and MBBY. (b-d) After applying the instrument response and differentiating the resulting synthetic velocity seismogram is band-passed (red dotted) and compared with the band-passed velocity seismogram (grey). The velocity seismograms are filtered between 0.001 and 0.05 Hz.

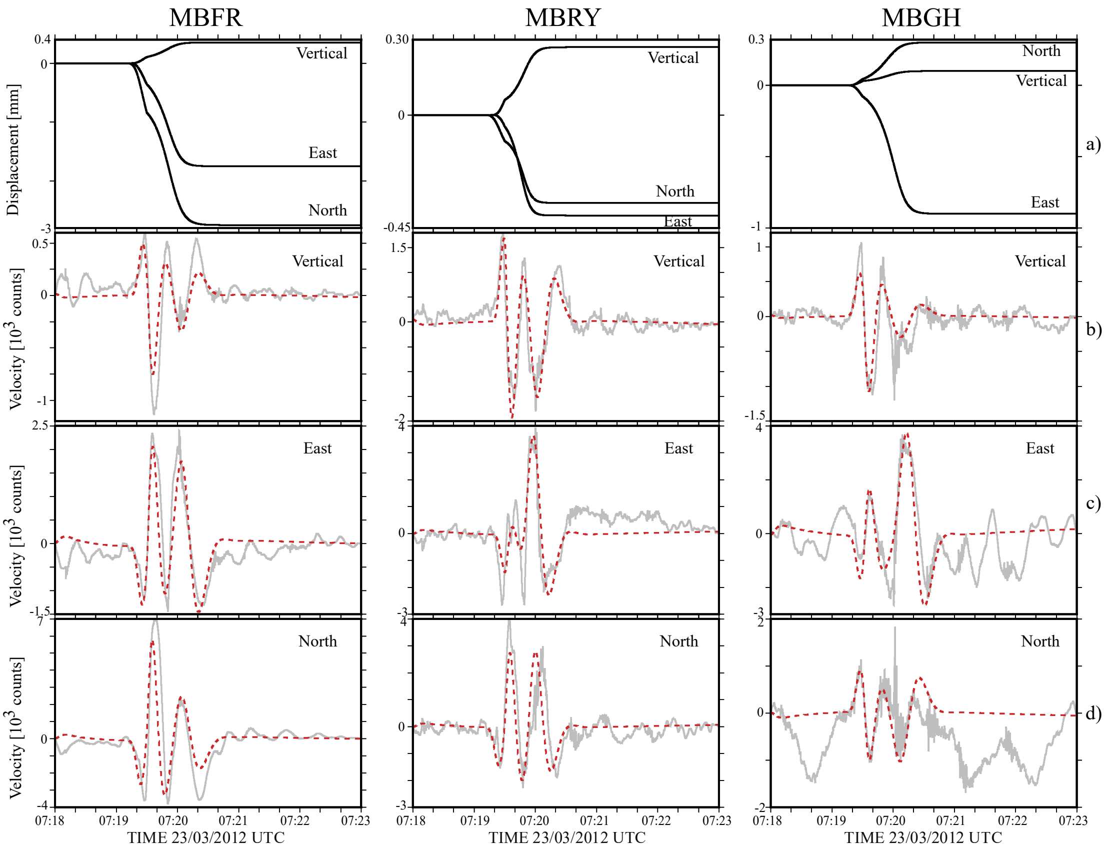

Figure 13: (a) Displacement models for all three components at stations MBFR, MBRY, and MBGH. (b-d) After applying the instrument response and differentiating the resulting synthetic velocity seismogram is band-passed (red dotted) and compared with the band-passed velocity seismogram (grey). The velocity seismograms are filtered between 0.001 and 0.05 Hz.